Design Aspects for a High-Precision Active Magnetic Bearing System

Gerald JUNGMAYR*, Robert SANTNER*, Dominik FRELLER*, Ryan NETRVAL**, Laura ROBERTS**, Aldo EJLLI** and Guido MUELLER**
* Linz Center of Mechatronics GmbH
Austria
** Max Planck Institute for Gravitational Physics
Germany

Abstract
Vacuum Magnetic Birefringence (VMB) is a subtle quantum electrodynamical effect predicted to induce a minute anisotropy in the vacuum refractive index in the presence of strong magnetic fields. Detecting this phenomenon requires highly sensitive polarimetric measurements under minimal vibrational disturbance. This paper presents the design and analysis of a high-precision active magnetic bearing (AMB) system intended to enable stable and low-vibration rotation of a permanent Halbach magnet for use in next-generation VMB experiments.
The paper identifies the dominant sources of mechanical vibrations in active magnetic bearing (AMB) systems. A dedicated magnetic bearing arrangement is proposed, consisting of actively controlled radial and axial bearings. The use of Bode's sensitivity integral highlights fundamental performance trade-offs in the control system and justifies the decision to implement active axial stabilization. A radial magnetic bearing design is shown and the number of coil windings is derived using an analytical design metric. Closed-loop simulations are used to evaluate the influence of ADC resolution for current and position sensing on control performance. The results demonstrate that higher ADC resolution significantly reduces RMS values of position and current, providing quantitative guidance for component specification.

Keywords : active magnetic bearing, precision, control, ADC, resolution, low vibration

1. Motivation

Vacuum Magnetic Birefringence (VMB) is a predicted optical phenomenon that arises from quantum electrodynamics (QED). The presence of strong magnetic fields affects polarized light, causing it to travel at varying speeds depending on the orientation of its polarization with respect to the magnetic field. Even with numerous experimental attempts to observe this phenomenon, detecting it hasn't proven easy, primarily because it requires extremely sensitive measurements.

Previous attempts employed pulsed and superconducting magnets. The most sensitive experiment to date, PVLAS [6], employed the mechanical rotation of permanent magnets mounted with ball bearings. However, at higher rotation frequencies, which are beneficial for improving signal-to-noise ratio, mechanical bearings introduce significant vibrational noise into the polarimetric detection system. This noise has so far prevented reaching the sensitivity required to conclusively verify VMB at the levels predicted by QED.

We investigate a design of an active magnetic bearing system capable of stable high-speed rotation with minimal mechanical vibration, aimed at enabling next-generation VMB detection. A central design goal is the minimization of vibrations that could interfere with precision polarimetry measurements.

2. Vacuum Magnetic Birefringence

QED predicts non-linear effects in vacuum. In the 1930s, Euler, Heisenberg, and Weisskopf derived a correction to

the classical electromagnetic Lagrangian [7, 10]:

$$\mathcal{L}_{\mathrm{EHW}} = \mathcal{L}_{\mathrm{cl}} + \frac{A_e}{\mu_0}\left[\left(\frac{E^2}{c^2} - B^2\right)^2 + 7\left(\frac{\mathbf{E}}{c}\cdot\mathbf{B}\right)^2\right], \quad A_e = \frac{2}{45\,\mu_0}\frac{\alpha^2\hbar^3}{m_e^4 c^5} = 1.32\times10^{-24}\ \mathrm{T}^{-2} \tag{1}$$

with m_e the electron mass and $\alpha = e^2/(4\pi\hbar c\epsilon_0)$ the fine structure constant. $\mathcal{L}_{\mathrm{cl}}$ is the classical electromagnetic Lagrangian density,

$$\mathcal{L}_{\mathrm{cl}} = \frac{1}{\mu_0}\left(\frac{E^2}{c^2} - B^2\right). \tag{2}$$

A key consequence is vacuum magnetic birefringence (VMB), where the vacuum acquires a tiny anisotropy in the presence of a strong magnetic field. Quantitatively, the birefringence is

$$\Delta n = n_{\parallel} - n_{\perp}\,, \tag{3}$$

where $n_{\parallel}$ and $n_{\perp}$ are the refractive indices for light polarized parallel and perpendicular to the external field, respectively. The accumulated phase shift for light propagating a distance L at wavelength λ is

$$\Delta\varphi = \frac{2\pi}{\lambda}\,L\,\Delta n. \tag{4}$$

For a plane wave propagating orthogonal to an external static magnetic field B_{ext}, the resulting birefringence is

$$\Delta n = 3A_e B_{\mathrm{ext}}^2 \approx 4\times10^{-24}\ \mathrm{T}^{-2}\cdot B_{\mathrm{ext}}^2. \tag{5}$$

A critical experimental challenge is that the predicted birefringence is extremely small. To detect the VMB signal against technical noise, it is advantageous to modulate the effect at a higher frequency. This is achieved by physically rotating the magnet, which shifts the signal away from low-frequency noise (e.g., $1/f$ electronics drift and environmental disturbances) and into a frequency band where the signal-to-noise ratio (SNR) is improved. The rotation frequency also sets the modulation frequency of the VMB signal, directly impacting the achievable sensitivity.

3. VMB Polarimeter

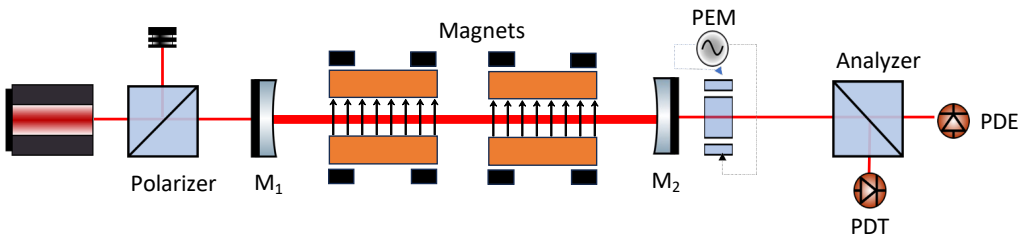

Fig. 1 Optical layout of the VMB polarimeter. From left to right: a linearly polarized laser beam passes a high-extinction polarizer, is injected into a Fabry–Pérot cavity formed by mirrors M_1 and M_2, traverses the vacuum region inside two rotating Halbach magnets (orange; arrows indicate the field direction), exits the cavity, and passes a photo-elastic modulator (PEM) operating at $\nu_m \approx 50$ kHz. The beam is then analyzed by a crossed polarizer; the extinguished port is detected on the ellipticity photodiode (PDE) while the transmitted port provides a reference signal on PDT.

The core of the polarimeter consists of a vacuum-compatible ceramic beam tube passing through two magnetically levitated, rotating permanent Halbach magnets. A laser beam, linearly polarized by a high-extinction polarizer, probes the magnetic-field region inside the tube and acquires an ellipticity due to VMB (Fig. 1). This ellipticity is modulated by the physical rotation of the magnets at frequency ν_B, so that the angle θ in the ellipticity formula,

$$\psi = \frac{\Delta\varphi}{2}\sin(2\theta) = \frac{\pi\Delta nL}{\lambda}\sin(2\theta), \tag{6}$$

varies continuously in time. Here, L is the optical path length in the magnetic field, λ is the wavelength, Δn is the birefringence, and θ is the angle between the input polarization and the magnetic field.

Both ends of the beam tube are terminated by high-reflectivity mirrors, forming a high-finesse Fabry–Perot optical cavity to enhance the interaction length. The resulting gain factor for the ellipticity amplitude is $N = 2\mathcal{F}/\pi$ where $\mathcal{F}$ is the cavity finesse.

To shift the VMB signal above low-frequency technical noise, a resonant photoelastic modulator (PEM) at frequency ν_m (typically 50 kHz) is placed after the cavity, modulating the acquired ellipticity. After passing through a crossed analyzer, the transmitted intensity at the photodetector (PDE) can be written as

$$I_{\perp}^{(\mathrm{ell})} = I_{\parallel} \left[\sigma^2 + \eta^2(t) + 2\eta(t) N\psi \sin 2\theta(t) + \ldots\right], \tag{7}$$

where $I_{\parallel}$ is the input intensity to the analyzer, σ^2 is the extinction ratio of the polarizers, and $\eta(t)$ is the ellipticity modulation produced by the PEM. The VMB-induced signal appears in the sidebands at $\nu_m \pm 2\nu_B$.

Demodulation at ν_m extracts the VMB ellipticity signal, which is proportional to the product of cavity gain, interaction length, and magnetic field. Various experiments have pursued this detection strategy, including those using pulsed, static, and rotating magnet configurations [3, 8, 6]. The most sensitive to date, PVLAS, achieved a normalized birefringence sensitivity of $\Delta n/B_{\mathrm{ext}}^2 = (19 \pm 27) \times 10^{-24}\ \mathrm{T}^{-2}$, but was limited by wideband noise attributed to thermal and Brownian motion in cavity mirror coatings [17, 16].

This wideband noise limits the achievable sensitivity, typically scaling with frequency as $f^{-\alpha}$, with $\alpha \approx 0.8$. The SNR for such a polarimeter can be estimated as [9]:

$$\mathrm{SNR} \propto \left(\frac{L}{1\,\mathrm{m}}\right)\left(\frac{B}{1\,\mathrm{T}}\right)^2\left(\frac{f}{1\,\mathrm{Hz}}\right)^{\alpha}. \tag{8}$$

This proportionality illustrates how higher fields and higher frequencies can improve sensitivity relative to a given baseline configuration. Note that the absolute SNR also depends on additional factors, intrinsic mirror birefringence amplitude, cavity dynamics, detection noise floor, and the small prefactor arising from the intrinsic vacuum birefringence amplitude, which are not shown explicitly here. A key bottleneck in previous PVLAS was the vibrational noise introduced by mechanical bearings, which constrained the achievable rotation (and hence modulation) frequencies. The use of active magnetic bearings enables stable, low-vibration rotation at frequencies up to several hundred hertz, providing a significant potential gain in sensitivity for future VMB searches. Demonstrating higher SNR with the magnetic-bearing prototype would already be a proof of principle showing that this approach is feasible. The concept could then be scaled by adding additional magnets to reach the sensitivity required for a definitive VMB measurement.

4. Comparison of continuous dipole field modulation concepts

The rotating magnetic field can be realized in three principal ways: (a) with a conventional three-phase stator (Fig. 2a); (b) with a single-phase coil driven by an H-bridge to produce an oscillatory dipole (Fig. 2b); and (c) with a permanently magnetized Halbach cylinder that is levitated and rotated in active magnetic bearings (Fig. 2c).

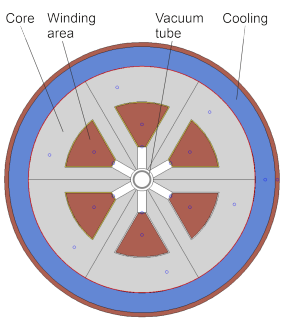

2a Three-phase system with distributed or concentrated windings.

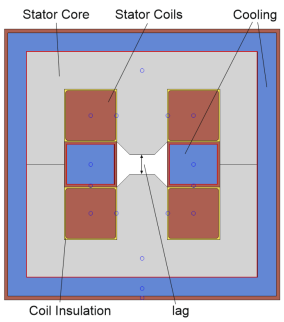

2b Single-phase system with enhanced cooling.

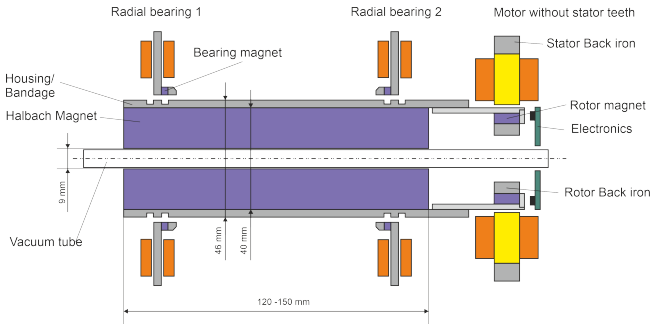

2c Proposed magnetic bearing setup for levitation and rotation of a Halbach magnet.

Fig. 2 Compared system variants for generating a high frequency dipole field

Freller *et al.* [9] optimized the coil-based options [*a*–*b*]. The resulting solution was compared to a rotating Halbach array supported by magnetic bearings [*c*].

In both stator configurations [*a*–*b*], the windings must be tuned with an external LC network to cancel reactive power, which locks the modulation to a single operating frequency. The magnetically levitated Halbach rotor, in contrast, produces the required 1.7 T dipole with much lower losses and reduces stator vibration by more than an order of magnitude through closed-loop control provided by the active magnetic bearings. Together, these benefits - lower losses, a freely selectable rotation frequency, and much better vibration performance - make the suspended Halbach array the preferred field generator for the VMB prototype.

5. Sources of vibration

Fig. 3 Sources of vibration in a magnetic bearing system (Icons from https://icons8.com).

Several mechanisms can contribute to unwanted vibrations in high-performance rotating systems, see Fig. 3. The aspects considered most critical by the authors for this project are marked with an asterisk. Understanding and addressing these effects is essential to ensure stable and precise operation of the AMB setup.

Rotor unbalance typically represents the dominant excitation force. This can be mitigated through accurate rotor balancing, where the rotor is already operated in the AMBs. To further suppress synchronous vibrations, generalized notch filters targeting the fundamental (1×) and especially the second harmonic (2×) of the rotational speed can be employed [5, 11]. The latter is particularly critical, as it coincides with the frequency of the VMB measurement signal, see eq. 6.

The rotor is optimized for high bending stiffness and operated subcritically with respect to its first bending mode.

Vibrations of the supporting structure can significantly amplify rotor oscillations. To mitigate this, the natural frequencies of the support structure should be carefully tuned to avoid resonance, with special attention to the second harmonic. Additionally, passive vibration isolation through the use of damping elements can provide further attenuation of structural modes.

Magnetic crosstalk between different components can induce undesirable forces and noise. It can be minimized by applying high-permeability shielding materials and by reducing magnetic leakage paths in both the motor and the magnetic bearings.

Reluctance forces vary with rotor angle and displacement, leading to torque ripple. These effects can be mitigated by

minimizing variations in magnetic reluctance, for example, through the use of a large air gap.

Asymmetrical motor currents are generated due to rotor or stator tolerances. Small deviations in the back EMF already lead to significantly unbalanced phase currents in high speed motors [15]. Minimizing such tolerances is crucial reduce force excitation induced by the motor stator.

Sensor noise and drift are critical issues for precision control. High-resolution ADCs help reduce quantization errors, which is further investigated in section 9. The shielding of sensor signals and the use of thermally stable electronic components enhance signal integrity. Well designed analog filters (in the electronics) and digital filters (in the control system) have to be used.

Manufacturing imperfections may cause sensor runout, degrading position measurement. This can be countered by high-precision manufacturing and careful assembly, as well as through calibration and compensation strategies in the control system, where runout maps are stored and applied.

Asymmetries in motor phase currents result in torque pulsations. These can be reduced by minimizing the dead time in power electronic switches (such as in half-bridge configurations) or using analog drivers, and by ensuring high-bandwidth current measurements for accurate control.

Temperature-induced deformation of components can alter alignment and stress distributions. Since cooling of the rotor is often limited, rotor losses should be minimized. Materials with low thermal expansion coefficients should be selected for the rotor and stator structures.

Finally, sensor–actuator collocation and the overall control architecture impact system performance. A decentralized control approach may offer improved robustness and decoupling [12].

6. Magnetic Bearing Setup

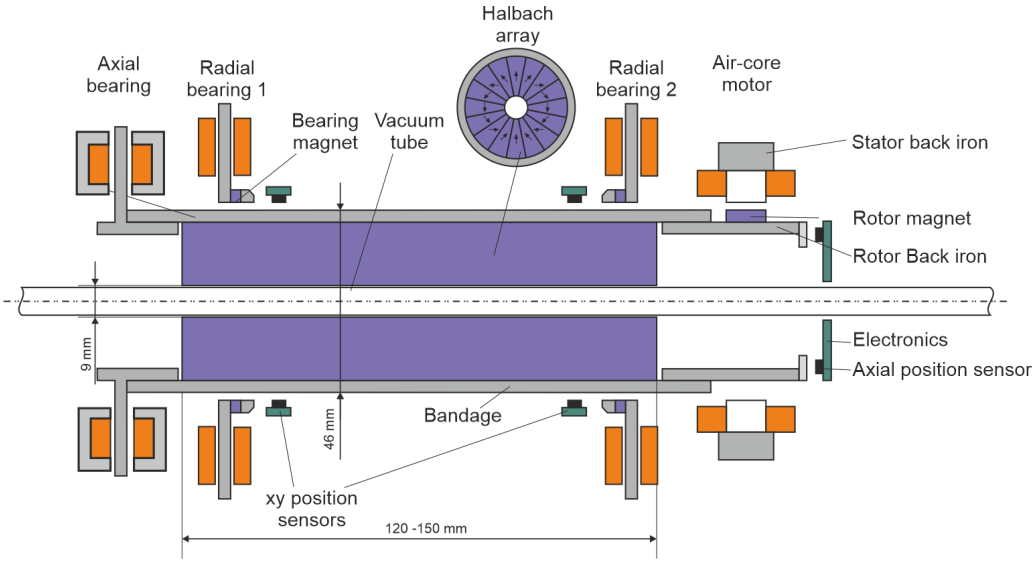

Fig. 4 Cross-section of the proposed magnetic bearing assembly

The topology of the planned magnetic bearing and motor system is shown in Fig. 4. A 16-segment Halbach array surrounds the ceramic vacuum tube and is radially supported by two active bearings (“Radial bearing 1” and “Radial bearing 2”). Axial stabilization is provided by a dedicated axial bearing, and torque is supplied by an air-core motor with a ferromagnetic stator back-iron. The outer sleeve acts as a housing/bandage and completes the flux return for the radial bearings. Typical prototype dimensions are indicated: 46 mm rotor OD, and 120 mm to 150 mm active length. The possibility of implementing passive axial stabilization was also explored, which would eliminate the need for an active axial bearing. However, the resulting increase in positive axial stiffness inherently causes a higher negative radial stiffness. As demonstrated in the next chapter, this negatively affects the sensitivity function.

7. Bode’s sensitivity integral applied to magnetic bearing system

Figure 5 shows the cascade structure of the investigated control for one degree-of-freedom (DOF). The direction

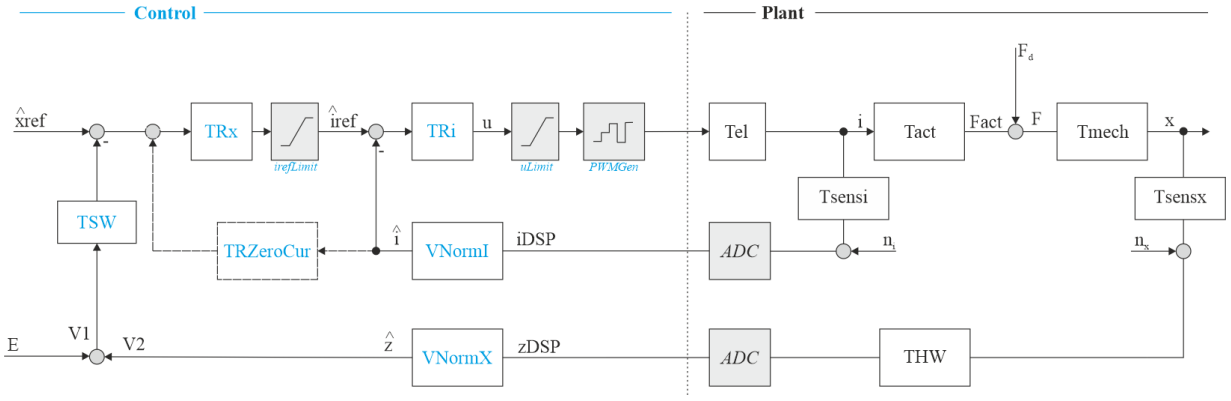

Fig. 5 Single-DOF AMB control loop. `TRi` closes the inner current loop through T_{el}; `TRx` closes the outer position loop through T_{act} and T_{mech}. Normalization blocks $V_{\mathrm{Norm}I}/V_{\mathrm{Norm}X}$, sensor low-pass filters $T_{\mathrm{HW}}/T_{\mathrm{SW}}$, and injection points E, V_1, V_2 support loop shaping and sensitivity measurement. Nonlinearities (current and voltage limit, ADC quantization and one-sample delay, PWM voltage generation) are indicated in grey.

represented by the variable x may correspond either to axial control or to one of the radial control axes. A high-bandwidth current controller `TRi` produces coil current i from a reference $\hat{i}_{\mathrm{ref}}$, while an outer position controller `TRx` acts on the measured rotor displacement x. An integrator in the `TRZeroCur` block can be used to determine the x-position at which the current is zero on average. `VNormI` and `VNormX` perform current and position normalization. `Tel`, `Tact`, and `Tmech` represent the electrical transfer function ($u \rightarrow i$), the force generation transfer function ($i \rightarrow F$), and the mechanical system ($F \rightarrow x$), respectively. `THW` denotes the hardware-implemented low-pass filters, while `TSW` comprises both notch and low-pass filters within the digital control system. The signals E, V_1, and V_2 define the injection points used for the digital measurement of the sensitivity function [1].

The nonlinearities in the system include the limitation of the current reference $i_{\mathrm{ref\,Limit}}$ and the voltage u_{Limit}, the quantization effects of the analog-to-digital converters (ADCs), and a one-sample delay T_s introduced by the digital control implementation.

In addition to the components already described, the block diagram includes further elements that increase the realism of the system model. A disturbance force F_d accounts for external mechanical excitations acting on the rotor, such as imbalances or vibrations. The transfer functions `Tsensx` and `Tsensi` represent the dynamics of the position and current sensing systems, respectively, including effects such as limited bandwidth. Additive noise components n_x and n_i are introduced after the respective sensor transfer functions.

A fundamental design constraint is expressed by Bode's sensitivity integral, also known as the "waterbed effect" [4][2]. In the following, nonlinear effects are neglected. The resulting transfer function of the plant $T_{\mathrm{act}} \cdot T_{\mathrm{mech}}$ is

$$P(s) = \frac{\hat{x}(s)}{\hat{i}(s)} = \frac{k_i/m}{s^2 - \omega_0^2}, \qquad \omega_0 = \sqrt{\frac{k_x}{m}}. \tag{9}$$

where m is the rotor mass, $k_i = T_{\mathrm{act}}$ is the current stiffness, and $k_x = -\frac{\partial F}{\partial x}$ is the (destabilizing) position stiffness. Thus $P(s)$ is a second-order system with one right-half-plane (RHP) pole at $+\omega_0$ and one left-half-plane (LHP) pole at $-\omega_0$.

The classical Bode sensitivity integral applies without modification to a single-axis AMB with an inner current loop. Its value is dictated solely by the plant's RHP pole at $+\omega_0$

$$\int_0^\infty \ln |S(j\omega)| \, \mathrm{d}\omega = \pi \sqrt{\frac{k_x}{m}} \tag{10}$$

where $S(s) = \frac{\hat{V}1(s)}{\hat{E}(s)}$ is the sensitivity function.

Hence the "waterbed area'' grows linearly with the open-loop natural frequency ω_0: stronger negative stiffness or lighter rotors worsen the unavoidable trade-off between low-frequency disturbance attenuation and high-frequency amplification. Equation (10) reveals a hard performance limitation: every suppression of load disturbances at low frequencies must be balanced by a peak in $|S(j\omega)|$ elsewhere. Controller design therefore amounts to shaping the frequency location and magnitude of this inevitable peak while keeping power amplifier limits and sensor noise in mind. Techniques such as lead compensation, notch filters, and μ–synthesis may shift and damp the peak but cannot reduce the total area prescribed by (10).

The impact of eddy currents on the sensitivity integral was analyzed in the work of Knospe and Zhu [14], where the performance limitations of non-laminated magnetic suspension systems were systematically examined.

8. Radial magnetic bearing

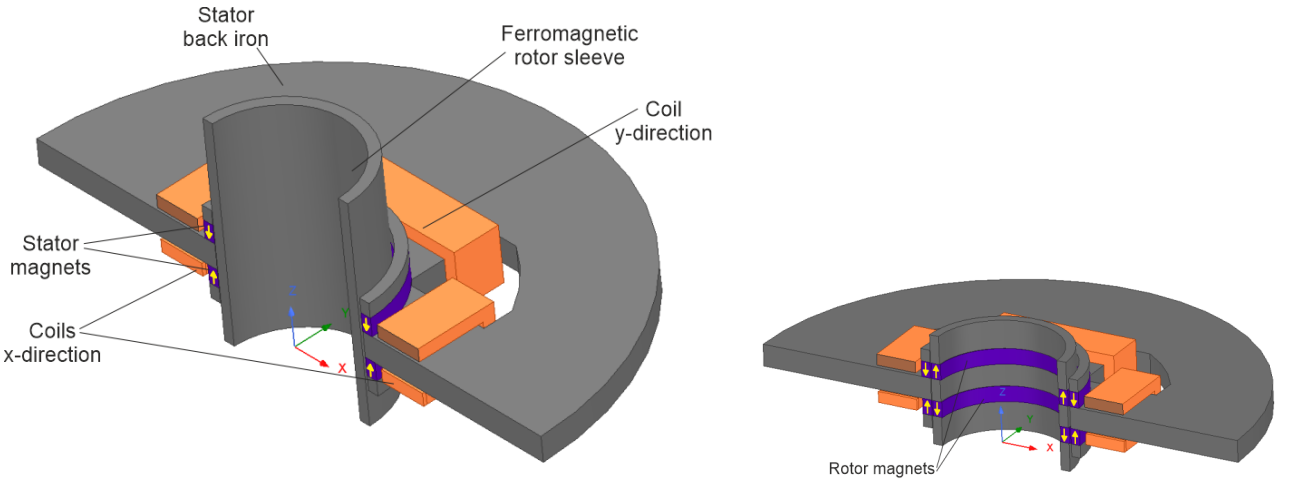

6a Cross section of radial magnetic bearing topology.

6b Design variant featuring rotor magnets to enhance axial stiffness.

Fig. 6 Solutions for radial magnetic bearing without and with rotor magnets

The topology of the radial magnetic bearing is shown in Fig. 6a. The stator of the radial magnetic bearing consists of four poles, each carrying one coil. Diametrically opposed coils are connected in series. Two permanent magnets integrated into the stator establish a homogeneous magnetic bias across the air gap.

To enhance axial stiffness, an additional permanent magnet may be mounted on the rotor (Fig. 6b). However, this also leads to increased dynamic instability in the radial directions. As shown, this has a negative influence on the sensitivity function in radial direction due to the Bode sensitivity integral.

Table 1 Parameters of the radial bearing

Parameter	**Value**
Rotor mass m	2.0 kg
Voltage U_{dc}	48 V
Touch down bearing clearance $x_{clearance}$	0.25 mm
Value of destabilizing stiffness k_x	238 N/mm
Number of windings per coil N	175 Wdg
Force per current k_i	47.4 N/A
Resistance R	6.22 Ω
Inductance L	69.8 mH
Dynamic start position $\frac{x_{0,max}}{x_{clearance}}$	0.80

The table 1 shows the parameters of the selected radial magnetic bearing design. The number of windings N was selected by looking at the metric $x_{0,stable}$. It is independent of the controller and can be calculated from the parameters listed in Table 1, see [13]. The maximum dynamic start position $x_{0,stable}$ describes the largest initial displacement from the equilibrium position at which a levitated mass can still be pulled back to the center (i.e. $x = 0\,\mu m$) by the AMB, given a delay-free startup and zero initial velocity. This value defines the maximum stabilization capability of the AMB and can be used to evaluate the dynamic performance of the AMB prior to the design of a controller.

In this paper we modify this metric as follows: we determine the initial position $x_{0,max}$ at which the rotor just barely avoids touching the mechanical stop $x_{clearance}$. The number of windings N was chosen by evaluation of the ratio $\frac{x_{0,max}}{x_{clearance}}$. If the rotor is positioned at $x = x_{0,max} = 200\,\mu m$ and the voltage is turned on at time $t = 0\,s$, the rotor can be brought back to the force free position $x = 0\,\mu m$, see Fig. 7.

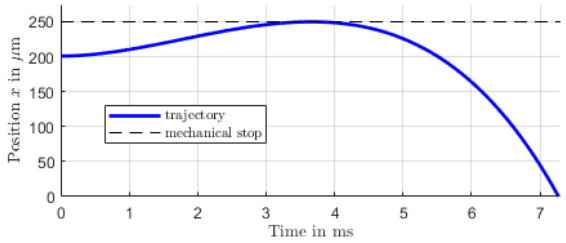

Fig. 7 Analytical calculation of the rotor position x when the maximum voltage is applied at $t = 0$ s. The starting position $x_{0,max}$ is defined as the point where the rotor reaches, but does not exceed, the mechanical stop.

9. Impact of ADC Resolution on control performance

This section examines the control of one radial degree of freedom, as illustrated in Figure 5. The investigation aims to determine how various parameters affect the quality of closed-loop control around the unstable equilibrium position at $x = 0\,\mu$m. Root mean square (RMS) values of position x and current i are evaluated as target variables. Notch filters - typically analyzed in `TSW` - are excluded from the present study.

Table 2 Nominal controller parameters

Parameter	Value
Position controller K_p	2.5
Position controller K_d	10×10^{-3}
Position controller f_c	3000 Hz
Current controller K_{pcur}	60
Software Position filter f_{cSW}	8 kHz
Harware Position filter 1 (Butterworth) f_{cHW1}	10 kHz
Harware Position filter 2 (first order) f_{cHW2}	15 kHz
Sampling time T_s	25 μs
PWM frequency f_{PWM}	40 kHz
ADC resolution position $N_{Bits,x}$	12
ADC resolution current $N_{Bits,i}$	12

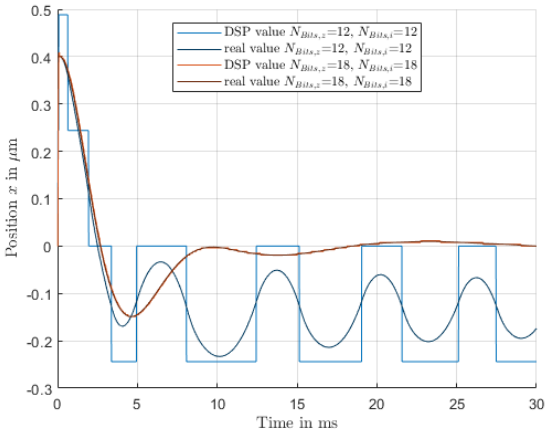

Fig. 8 Position (real and quantized) for a coarse 12-bit and a fine 18-bit ADC resolution

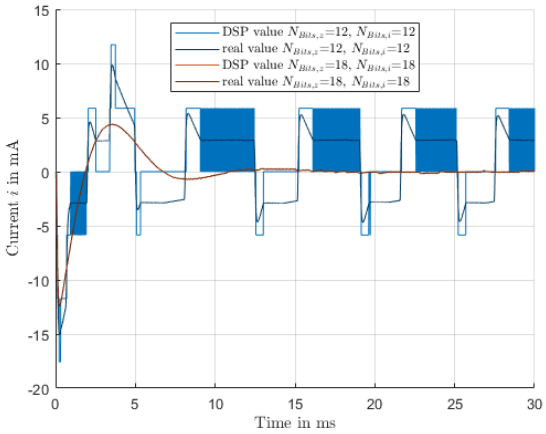

Fig. 9 Current (real and quantized) for a coarse 12-bit and a fine 18-bit ADC resolution

The nominal parameters of the bearing and controller are provided in Tables 1 and 2. The controller parameters were determined by simulating the sensitivity function $S(j\omega)$.

Two half bridges are controlled using a center-aligned pulse width modulation (PWM) with a nominal frequency of $f_{PWM} = 40$ kHz and soft chopping. The best-case scenario without added noise is simulated using a time-stepping

closed-loop simulation. Only the quantization effects of the position and current ADCs are considered, as well as the delay caused by the digital control.

Fig. 8 shows the simulated position response for a small initial deflection of $x = 0.4\,\mu$m, comparing a 12-bit and an 18-bit DSP resolution applied to both position and current measurements. It can be observed that, with the 12-bit ADC, only the least significant bit of the position measurement continues to change. A resolution increase from 12 to 18 bits in the ADC yields more than 20 dB attenuation in position and current signals. However, this assumes that the measurement noise with an 18 bit ADC is still smaller than the quantization level.

Figures 10 and 11 show the RMS values of position and the current for different ADC resolutions $N_{Bits,x}$ and $N_{Bits,i}$. For this purpose, the RMS value was calculated using only the second half of the simulated signal, specifically from 15 ms to 30 ms. Fig. 11 shows that an increasing the number of ADC bits for position reduces the RMS value for current, provided that the ADC resolution for current is also increased. However, the difference between $N_{Bits,i} = 18$ and $N_{Bits,i} = 20$ is negligible.

Subsequently, additional parameters of the control loop were varied to analyze the sensitivity of the RMS value of position and current with respect to each parameter. For the studied magnetic bearing it was observed that, unlike the ADC resolution $N_{Bits,x}$ and $N_{Bits,i}$, the sampling time T_s, PWM resolution f_{PWM} and number of turns N had a significantly smaller influence on these parameters.

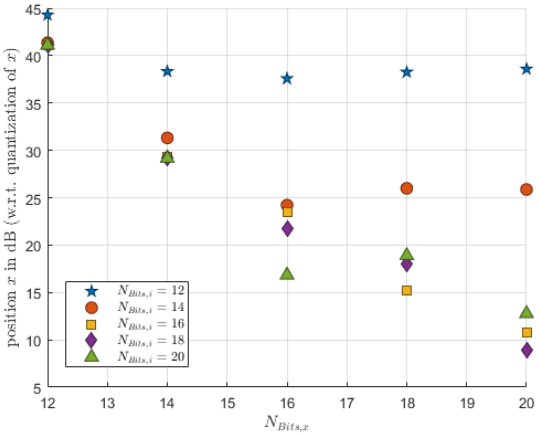

Fig. 10 Influence of ADC resolution $N_{Bits,x}$ and $N_{Bits,i}$ on RMS value of position

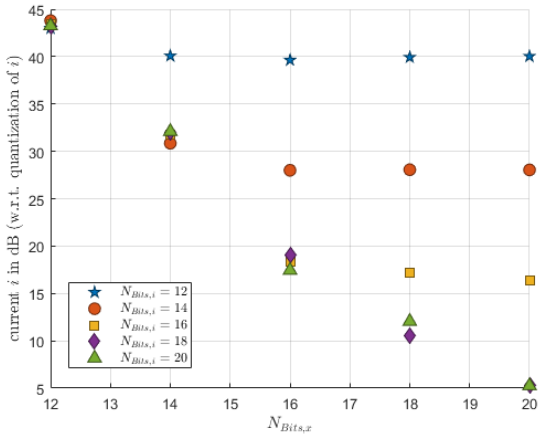

Fig. 11 Influence of ADC resolution $N_{Bits,x}$ and $N_{Bits,i}$ on RMS value of current

10. Summary and outlook

This paper presented the design and analysis of a high-precision active magnetic bearing (AMB) system tailored for low-vibration rotation in next-generation Vacuum Magnetic Birefringence (VMB) experiments. A dedicated bearing topology with actively controlled radial and axial degrees of freedom was introduced. An analytical design metric was employed to select the number of coil windings independently of the controller. Closed-loop simulations revealed that ADC resolution is the primary factor affecting control performance, provided that sensor noise is lower than quantization noise. By comparison, parameters such as PWM frequency, sampling time, and number of turns exert only minor effects in the investigated system. The next steps include the detailed design of the magnetic bearings, the motor, the overall mechanical structure, as well as the signal and power electronics. To validate these simulation results, experimental measurements will be carried out on the prototype system.

11. Acknowledgment

This work was carried out at LCM GmbH as part of a K2 project. K2 projects are financed using funding from the Austrian COMET-K2 program. The COMET-K2 projects at LCM are supported by the Austrian federal government, the federal state of Upper Austria, Johannes Kepler University Linz, and all partners that form part of the COMET-K2 consortium.

References

[1]ISO 14839. *Mechanical vibration — Vibration of rotating machinery equipped with active magnetic bearings*. 2006.

[2]Karl J. Aström. *Feedback Systems*. URL: https://www.cds.caltech.edu/~murray/amwiki/.

[3]R. Battesti et al. "The BMV experiment: a novel apparatus to study the propagation of light in a transverse magnetic field". en. In: *The European Physical Journal D* 46.2 (Feb. 2008), pp. 323–333. ISSN: 1434-6079. DOI: 10.1140/epjd/e2007-00306-3. URL: https://doi.org/10.1140/epjd/e2007-00306-3 (visited on 06/12/2025).

[4]Hendrik W. Bode. *Network Analysis and Feedback Amplifier Design*. D. Van Nostrad Company, 1945.

[5]Guzman Borque Gallego et al. "Novel Generalized Notch Filter for Harmonic Vibration Suppression in Magnetic Bearing Systems". In: *IEEE Transactions on Industry Applications* 57.6 (Nov. 2021), pp. 6977–6987. ISSN: 0093-9994, 1939-9367. DOI: 10.1109/TIA.2021.3062587. URL: https://ieeexplore.ieee.org/document/9364732/ (visited on 05/06/2025).

[6]A. Ejlli et al. "The PVLAS experiment: A 25 year effort to measure vacuum magnetic birefringence". In: *Physics Reports* 871 (Aug. 2020), pp. 1–74. ISSN: 03701573. DOI: 10.1016/j.physrep.2020.06.001. URL: https://linkinghub.elsevier.com/retrieve/pii/S0370157320302428 (visited on 10/09/2024).

[7]H. Euler and B. Kockel. "Über die Streuung von Licht an Licht nach der Diracschen Theorie". de. In: *Naturwissenschaften* 23.15 (Apr. 1935), pp. 246–247. ISSN: 1432-1904. DOI: 10.1007/BF01493898. URL: https://doi.org/10.1007/BF01493898 (visited on 06/02/2025).

[8]Xing Fan et al. "The OVAL experiment: a new experiment to measure vacuum magnetic birefringence using high repetition pulsed magnets". en. In: *The European Physical Journal D* 71.11 (Nov. 2017), p. 308. ISSN: 1434-6079. DOI: 10.1140/epjd/e2017-80290-7. URL: https://doi.org/10.1140/epjd/e2017-80290-7 (visited on 06/12/2025).

[9]Dominik Freller et al. "High Frequency Dipole Magnetic Field for Vacuum Magnetic Birefringence". In: *11th ECCOMAS Thematic Conference on Smart Structures and Materials*. 11th ECCOMAS Thematic Conference on Smart Structures and Materials. Linz, Austria, July 2025, p. 11.

[10]W. Heisenberg and H. Euler. "Folgerungen aus der Diracschen Theorie des Positrons". de. In: *Zeitschrift für Physik* 98.11 (Nov. 1936), pp. 714–732. ISSN: 0044-3328. DOI: 10.1007/BF01343663. URL: https://doi.org/10.1007/BF01343663 (visited on 06/02/2025).

[11]R. Herzog et al. "Unbalance compensation using generalized notch filters in the multivariable feedback of magnetic bearings". In: *IEEE Transactions on Control Systems Technology* 4.5 (Sept. 1996), pp. 580–586. ISSN: 10636536. DOI: 10.1109/87.531924. URL: http://ieeexplore.ieee.org/document/531924/ (visited on 03/12/2025).

[12]Markus Hutterer. "Regelung von magnetgelagerten Rotoren für den Einsatz in Turbomolekularpumpen". Artwork Size: 145 pages Medium: application/pdf Pages: 145 pages. PhD thesis. TU Wien, 2018. DOI: 10.34726/HSS.2018.47282. URL: https://repositum.tuwien.at/handle/20.500.12708/1800 (visited on 12/09/2024).

[13]Gerald Jungmayr et al. "Characteristic Quantities of Active Magnetic Bearings". In: *ISMB15, 15th International Symposium on Magnetic Bearings, Kitakyushu, Japan, August 3.-6, 2016*. Aug. 2016, p. 7. URL: http://www.ismb15.org/.

[14]Carl R. Knospe and Lei Zhu. "Performance Limitations of Non-Laminated Magnetic Suspension Systems". In: *IEEE Transactions on Control Systems Technology* 19.2 (Mar. 2011), pp. 327–336. ISSN: 1063-6536, 1558-0865. DOI: 10.1109/TCST.2010.2044179. URL: http://ieeexplore.ieee.org/document/5463016/ (visited on 06/02/2025).

[15]Jie Song et al. "Position and speed estimation for high speed permanent magnet synchronous motors using wideband synchronous fundamental-frequency extraction filters". In: *Journal of Power Electronics* 22.2 (Feb. 1, 2022), pp. 254–265. ISSN: 2093-4718. DOI: 10.1007/s43236-021-00356-z. URL: https://doi.org/10.1007/s43236-021-00356-z.

[16]Shi-Xiang Yang et al. "Study of the birefringence noise in high-finesse ULE cavity". In: *Optics & Laser Technology* 181 (Feb. 2025), p. 111660. ISSN: 0030-3992. DOI: 10.1016/j.optlastec.2024.111660. URL: https://www.sciencedirect.com/science/article/pii/S0030399224011186 (visited on 06/02/2025).

[17]G. Zavattini et al. “Intrinsic mirror noise in Fabry-Perot based polarimeters: the case for the measurement of vacuum magnetic birefringence”. In: *The European Physical Journal C* 78.7 (July 2018), p. 585. ISSN: 1434-6044, 1434-6052. DOI: 10.1140/epjc/s10052-018-6063-y. arXiv: 1805.03198[physics]. URL: http://arxiv.org/abs/1805.03198 (visited on 06/06/2025).